Check for updates

JGR Space Physics

RESEARCH ARTICLE
10.1029/2026JA035200

Special Collection:
Coupling Processes from Space to Earth

Peculiar Magnetosphere-Atmosphere Coupling and Its Impacts Over the South American Magnetic Anomaly Region

Lígia A. Da Silva[1,2,3], Hui Li[1,3], Laysa C. A. Resende[1,2,3], Vânia F. Andrioli[1,2,3], Angela M. Santos[1,2,3], Juliano Moro[1,3,4], Paulo R. Jauer[1,2,3], Luis Eduardo Vieira[2], Lívia R. Alves[2], José Paulo Marchezi[2], Jiankui Shi[1,3], Jiyao Xu[1,2], Paulo P. Batista[2], Jose V. Bageston[4], Yajun Zhu[1,3], Clezio M. Denardini[2], Chi Wang[1,3], Ezequiel Echer[2], Guotao Yang[1,3], Alexandre A. Pimenta[2], Joaquim R. Costa[2], and Zhengkuan Liu[1,3]

[1]State Key Laboratory for Space Weather, National Space Science Center, Chinese Academy of Sciences, Beijing, China, [2]National Institute for Space Research (INPE), São José dos Campos, Brazil, [3]China-Brazil Joint Laboratory for Space Weather, NSSC/INPE, São José dos Campos, Brazil, [4]National Institute for Space Research (INPE), Santa Maria, Brazil

Key Points:

- The magnetosphere-atmosphere coupling conditions contributed to atypical electron precipitation over the SAMA region
- The absence of hiss and MS waves in the 40–200 Hz frequency range changes the altitude of the ionization rate integrated peak over SAMA
- The peculiar altitude of the ionization rate integrated peak over the SAMA defines the altitude of this peculiar layer

Supporting Information:

Supporting Information may be found in the online version of this article.

Correspondence to:

L. A. Da Silva,
ligia.silva@inpe.br

Citation:

Da Silva, L. A., Li, H., Resende, L. C. A., Andrioli, V. F., Santos, A. M., Moro, J., et al. (2026). Peculiar magnetosphere-atmosphere coupling and its impacts over the South American Magnetic Anomaly region. *Journal of Geophysical Research: Space Physics*, *131*, e2026JA035200. https://doi.org/10.1029/2026JA035200

Received 5 FEB 2026
Accepted 6 AUG 2026

© 2026 The Author(s). Journal of Geophysical Research: Space Physics published by Wiley Periodicals LLC on behalf of American Geophysical Union. This is an open access article under the terms of the Creative Commons Attribution License, which permits use, distribution and reproduction in any medium, provided the original work is properly cited.

Abstract The auroral-like sporadic E-layer is typically observed at altitudes between 100 and 150 km within the South American Magnetic Anomaly region. However, the occurrence of an unusual layer event detected above this altitude range on 18 July 2017 has raised intriguing questions regarding the physical processes responsible for the substantial vertical displacement of this layer. The interplanetary medium conditions during the event exhibited characteristics consistent with the recovery phase of a geomagnetic storm driven by a complex solar wind structure, occurring after substorm activity. To address this atypical layer occurrence, we examined the magnetospheric conditions using the BATS-R-US model with two experiments: one including the actual geomagnetic dipole inclination and another omitting it. These configurations allow for a discussion of the energy deposition processes under the prevailing interplanetary medium conditions. Also, the dynamics of the inner radiation belt were investigated through analysis of the magnetic field power spectral density and low-energy electron flux measurements from the Van Allen Probes mission to verify electron precipitation. Plasma wave observations and their characterization also revealed atypical behavior, in which a non-standard confinement of hiss waves (200 and 500 Hz) occurred simultaneously with an electron flux decrease (<1 keV), an integrated ionization rate between 250 and 300 km, and the formation of a peculiar layer. Finally, although this magnetic storm was moderate, we demonstrate that particle precipitation significantly impacted the atmosphere, as evidenced by pronounced ozone depletion in the mesosphere with magnitudes substantially stronger when compared to the extreme storm of May 2024.

1. Introduction

The coupling between the magnetosphere and atmosphere during space weather events is a topic of significant interest in the scientific community. Events such as Coronal Mass Ejections (CMEs) and High-Speed solar wind Streams (HSSs) impact the neutral and ionized components of the atmosphere differently, often leading to anomalous behavior (Da Silva et al., 2022, 2023a). In particular, rapid southward variations of the Interplanetary Magnetic Field (IMF) Bz component can allow disturbed electric fields to influence ionospheric dynamics on a global scale. Additionally, enhancements in radiation belt particle populations, as well as their subsequent precipitation into the atmosphere, can significantly impact multiple ionized and neutral atmosphere regions. These effects include disturbances in the *D* (60–90 km) and E-regions (90–150 km) of the ionosphere, modifications in ozone distributions within both the Mesosphere and Lower Thermosphere (MLT) regions (80–100 km) and the Mesosphere region (60–80 km), as well as changes in the formation and characteristics of sporadic E (Es) layers (100–150 km).

The inner and outer radiation belts, located in L-shells between ∼1 and 2 RE and ∼3.5–6.5 RE (Earth radii–RE), respectively, are composed preferentially of electrons and protons, respectively, spanning a wide range of energies that undergo adiabatic motion along magnetic field lines (Northrop & Teller, 1960; Roederer, 1970). Particle dynamics in these belts are strongly influenced by the presence of magnetospheric waves, such as whistler-mode chorus, electromagnetic ion cyclotron (EMIC), magnetosonic (MS), and plasmaspheric hiss waves, which drive particle scattering (Alves et al., 2016; Da Silva et al., 2021a, 2022, 2023a; Nakamura

21699402, 2026, 8, Downloaded from https://agupubs.onlinelibrary.wiley.com/doi/10.1029/2026JA035200 by Center For Space Science And Applied Research, CAS, Wiley Online Library on [19/11/2026]. See the Terms and Conditions (https://onlinelibrary.wiley.com/terms-and-conditions) on Wiley Online Library for rules of use; OA articles are governed by the applicable Creative Commons License

et al., 2019; Turner et al., 2014) and acceleration (Alves et al., 2024; Da Silva et al., 2021b, 2023b; Li et al., 2015) processes. These interactions lead to variability in the competing source and loss mechanisms, with effects becoming particularly pronounced during geomagnetic disturbances (Horne et al., 2009; Turner et al., 2019). The slot region between the inner and outer belts, typically characterized by reduced particle density, and the plasmasphere can undergo significant modifications during magnetic storms, altering particle transport and wave-particle interactions. Moreover, the specific response of energetic particles depends strongly on the nature of the driving solar wind structure. During CMEs, for example, enhanced ring current and strong southward Bz components can result in strong and faster particle injections (Da Silva et al., 2023b) and shorter atmospheric losses, whereas HSSs often produce slower and more gradual enhancements with prolonged precipitation rates into the atmosphere (Da Silva et al., 2021b).

The effects of electron particle precipitation (EPP) on the atmosphere have been extensively studied at auroral stations, where measurements of electron and proton fluxes enable detailed analyses of these interactions. Duderstadt et al. (2021) quantified enhancements of atmospheric odd nitrogen (NOx) and odd hydrogen (HOx), and the resulting depletion of ozone (O_3) in the middle atmosphere using observations from the NASA Van Allen Probes and NSF's Focused Investigations of Relativistic Electron Burst Intensity, Range, and Dynamics (FIREBIRD II) CubeSats. The authors presented a March 2013 case study in which they observed intense and prolonged electron loss from the outer radiation belt during the recovery phase of a moderate geomagnetic storm. While electron loss during the main phase of storms is generally attributed to escape through the magnetopause, much of the decay observed in this sustained event was associated with precipitation into the atmosphere.

More recently, Murase et al. (2025) investigated the interactions between electrons and EMIC waves during particle precipitation over auroral stations. Using a combination of imaging riometer, magnetometer, and radar data, they found that precipitation predominantly occurred on the noon-dusk side between 12:00 and 18:00 MLT. Approximately 70% of these events were accompanied by ionization signatures at altitudes above 60 km, supporting the interpretation that sub-MeV electron precipitation (EEPs) was primarily driven by resonant scattering with EMIC waves.

Over the Brazilian sector lies the South American Magnetic Anomaly (SAMA), characterized by unusually low magnetic field values that facilitate particle precipitation. Unlike auroral regions, where precipitation is primarily driven by solar wind-magnetosphere interactions, particles in the SAMA originate from the inner radiation belts and generally have lower energy levels. Two main processes govern particle precipitation in this region. The first is a continuous process associated with the displacement of the inner boundary of the inner radiation belt (Roederer, 1970), which shifts the magnetic mirror point in this region to low altitudes (around 100 km), thereby promoting strong collisional interactions between the trapped charged particles and the neutral atmosphere composition. The second involves processes related to the precipitation of low-energy electrons (Batista & Abdu, 1977; Da Silva et al., 2022, 2023a; Moro et al., 2022, Resende et al., 2024). This mechanism, known as collisional or Coulomb scattering, can be intensified during the initial or main phases of magnetic storms (Resende et al., 2024). The second process involves interactions between energetic electrons and magnetospheric waves. Resonant interactions can break the first and/or second adiabatic invariants of particle motion, allowing electrons to enter the loss cone and precipitate into the atmosphere (Alves et al., 2016; Bittencourt, 2004; Da Silva et al., 2019, 2023a, 2025).

Studying the particle precipitation over the SAMA region remains challenging because of limited observational data, particularly due to the proton contamination (e.g., Andersson et al., 2014; Rodger et al., 2013). Early work by Batista and Abdu (1977) provided the first evidence that the Brazilian ionosphere within the SAMA, over Cachoeira Paulista–SP (Lat: 22°39′54″S, Lon: 45°00′34″W), can exhibit auroral-like behavior, identifying spreading-type ionogram traces near 100 km that were termed the auroral sporadic layer (Esa). More recently, Da Silva et al. (2022, 2023a) analyzed comparable traces in ionograms collected in Santa Maria–RS (Lat: 29°68′40″ S, Lon: 53°80′61″W), Brazil, at the same altitude and supported by satellite observations, and concluded that the Esa layer at Brazilian stations is driven by resonant interactions between electrons and hiss waves during the recovery phase of magnetic storms. Because both Cachoeira Paulista and Santa Maria lie near the center of the SAMA, the results of Da Silva et al. (2022) align with those of Moro et al. (2022) and Da Silva et al. (2023a), which also reported signatures of particle precipitation over the region during other geomagnetic storm events.

Additionally, Da Silva et al. (2025) investigated the extreme geomagnetic storm of 10–11 May 2025 and documented its effects throughout the neutral and ionized atmosphere. Among their findings, the authors reported

notable changes in mesospheric ozone (80–100 km), including an abrupt ozone depletion over the SAMA that occurred simultaneously with variability in inner-radiation-belt electron fluxes. For the same storm, Resende et al. (2024) demonstrated that particle precipitation induced atmospheric oscillations through Joule heating, leading to the first reported nighttime occurrence of a cusp-sporadic E layer (Es_c), a phenomenon typically observed only during the daytime.

In this context, the present study investigates the effects of an anomalous episode of hiss wave activity in the magnetosphere observed when the Van Allen Probes passed over an ionosonde station located in the SAMA region during the geomagnetic storm of 18 July 2017. The disturbance produced a pronounced irregularity in the ionized atmosphere, manifested as a spread-type trace near 250 km, a feature that resembles the auroral Es layer but occurred at an altitude where such signatures had never previously been reported. The modeled ionization rate during the detection of the anomalous layer revealed that the precipitating electron flux influenced the ionosphere in distinct height-dependent ways, indicating that the energy distribution and penetration of the electrons varied significantly with altitude. Furthermore, concurrent ozone depletion was detected, confirming that particle precipitation impacted the atmosphere. Together, these findings address key open questions regarding how magnetospheric hiss waves interact with energetic particles in the inner radiation belt and how this interaction couples to the neutral and ionized atmosphere over the SAMA region.

2. Data Set and Methodology

The coupling between solar wind structures and the Earth's magnetosphere has been widely studied by the scientific community (Echer et al., 2008; Gonzalez et al., 2011; and therein). However, the physical processes within the inner magnetosphere that drive space weather impacts in the atmosphere, particularly over the SAMA region, are still not fully understood (Borovsky, 2018; Borovsky & Yakymenko, 2017; Da Silva et al., 2025). Under the influence of solar wind structures, the ionosphere within the SAMA region may exhibit auroral-like behavior at low geomagnetic latitudes (Da Silva et al., 2022, 2023a, 2025; Moro et al., 2022; Resende et al., 2024; Santos et al., 2016), motivating a combined analysis of interplanetary, magnetospheric, ionospheric, and atmospheric observations.

Solar wind conditions during the analyzed interval were characterized using magnetic field and plasma data at the Earth's bow shock nose obtained from the Magnetic Field Experiment (MAG) and Solar Wind Electron, Proton, and Alpha Monitor (SWEPAM) instruments onboard the ACE satellite (Stone et al., 1998) available at https://omniweb.gsfc.nasa.gov/form/omni_min_def.html. The storm and substorm conditions at the magnetosphere are analyzed using geomagnetic indices, including SYM-H and AE, which are computed at WDC for Geomagnetism (https://wdc.kugi.kyoto-u.ac.jp/aeasy/) and available at https://omniweb.gsfc.nasa.gov/form/omni_min_def.html.

The coupling between the solar wind and the magnetosphere was modeled globally using the three-dimensional magnetohydrodynamic (MHD3D) approximation. The inner magnetosphere region includes coupling with two additional internal models: the Inner Magnetosphere (IM) and the Ionosphere Electrodynamics (IE) modules. The MHD3D framework enables a comprehensive understanding of the global magnetospheric state before, during, and after the analyzed interval. For this purpose, three components of the Space Weather Modeling Framework (SWMF) and Block- Adaptive Tree Solar wind Roe-type Upwind Scheme (BATS-R-US) were coupled: the Global Magnetosphere (GM) module (Gombosi et al., 2001, 2003, 2021; Powell et al., 1999; Tóth et al., 2005, 2012 and references therein), the Inner Magnetosphere (IM) module based on the Rice Convection Model (RCM) (Toffoletto et al., 2003), and Ionosphere Electrodynamics (IE) module (Ridley et al., 2006). The SWMF/BATS-R-US model, developed at the University of Michigan in the Center for Space Environment Modeling (CSEM), is available through the NASA Community Coordinated Modeling Center (CCMC). The model configuration, including the simulation domain, Pedersen conductivity, temperature, and density at the inner boundary, followed the same procedure described by Jauer et al. (2019, 2022).

Inner magnetosphere conditions are analyzed using Van Allen probe B (VAP-B) data (Mauk et al., 2013), in which the electron flux energy levels between 10 eV and 50 keV variability and plasma wave activity within the inner radiation belt are observed using the Helium, Oxygen, Proton, and Electron (HOPE) instrument (Funsten et al., 2013), and the Electric and Magnetic Field Instrument Suite and Integrated Science (EMFISIS) instrument (Kletzing et al., 2013), respectively. The Power Spectral Density (PSD), total electron density, ellipticity, and planarity of the plasmaspheric hiss and magnetosonic (MS) waves were estimated and analyzed to study the

21699402, 2026, 8, Downloaded from https://agupubs.onlinelibrary.wiley.com/doi/10.1029/2026JA035200 by Center For Space Science And Applied Research, CAS, Wiley Online Library on [19/11/2026]. See the Terms and Conditions (https://onlinelibrary.wiley.com/terms-and-conditions) on Wiley Online Library for rules of use; OA articles are governed by the applicable Creative Commons License

21699402, 2026, 8, Downloaded from https://agupubs.onlinelibrary.wiley.com/doi/10.1029/2026JA035200 by Center For Space Science And Applied Research, CAS, Wiley Online Library on [19/11/2026]. See the Terms and Conditions (https://onlinelibrary.wiley.com/terms-and-conditions) on Wiley Online Library for rules of use; OA articles are governed by the applicable Creative Commons License

scenario of the inner radiation belt. These analyses within the inner radiation belt use the VAP-B at the perigee orbit, particularly crossing the SAMA, as shown in Figure SI1 of Supporting Information S1, to infer the possible wave-particle resonance occurrence during the detection of a peculiar Es layer in the study.

Typical Es layers or intermediates in the ionized atmosphere are a thin ionization layer that forms below the F region between 90 and 150 km altitude (Haldoupis, 2011; Mathews, 1998; Resende et al., 2017). To detect the Es layer over the SAMA region, we use the ionospheric data collected by the Digisonde-Portable-Sounder-4D (DPS4D) (Lowell Digisonde International, University of Massachusetts Lowell) installed over the low latitude station of Cachoeira Paulista, which operates as a high-frequency (HF) radar transmitting short radio pulses into the ionosphere over a 1–30 MHz range. This instrument employs four crossed receiving antennas to infer the direction of arrival of echoes via phase comparison, enabling full three-dimensional characterization of plasma motions. The DPS-4D measures the time delay, Doppler shift, and angle of arrival of the reflected echoes to derive ionograms, plasma drift velocities, and sky maps. From the ionograms, the system provides the virtual height and critical frequencies of the ionospheric layers (e.g., h′F2, foE, and foF2). Data are recorded automatically at regular intervals (every 10 min for Cachoeira Paulista) and processed using the Automatic Real-Time Ionogram Scaler with True Height (ARTIST) autoscaling algorithm to generate the SAO (Standard Archiving Output) data files used in this study (Reinisch et al., 2009). In this work, we investigate an atypical Es-layer trace, which we refer to as an intermediate layer because it is located between the conventional E and F regions. Intermediate layers can occur at these altitudes and are commonly associated with localized enhancements in ionization, as reported in the literature (e.g., Dos Santos et al., 2019; Santos et al., 2020, 2022). Therefore, when such layers appear at higher altitudes and exhibit auroral-like characteristics, they may be regarded as peculiar ionospheric features. The physical mechanisms responsible for their formation are still not fully understood, particularly over the SAMA region, and therefore warrant special attention when such events are observed.

The atmospheric ionization rate over the center of the SAMA region during the detection of an atypical layers is estimated using an empirical model that the parameterization of ionization in the atmosphere is driven by the isotropically precipitating monoenergetic (100 eV–1 MeV) electrons (Fang et al., 2010). This model computes the atmospheric ionization at Cachoeira Paulista, assuming that the incident particles, given by differential number flux (cm^{-2} s^{-2} keV^{-1}), have a Maxwellian distribution, as described in Fang et al. (2010) and Da Silva et al. (2022).

To confirm the occurrence of EPP over the SAMA region, we also analyzed the ozone distribution within the mesosphere and MLT altitudes during the event in the study using the data from the Sounding of the Atmosphere using Broadband Emission Radiometry (SABER) instrument on board the TIMED (Thermosphere, Ionosphere, Mesosphere, Energetics, Dynamics) satellite (Russell et al., 1999). The SABER instrument uses a 10-channel broadband limb-scanning infrared radiometer covering the spectral range from 1.27 to 17 μm from several atmospheric species, including O_3 (1.27 and 9.6 μm), in which the volume mixing ratio in the 9.6 μm channel is used here. For details of the SABER retrieval algorithm, see Rong et al. (2009). We considered a grid of 10° on latitude and 20° on longitude, from 30°S to 20°S and 40°W to 60°W, which covers the SAMA center.

3. Results and Discussions

3.1. Atypical Auroral-Like Es Layer Signature Over the SAMA

The ionograms in Figure 1 show the appearance of a spread layer trace at Cachoeira Paulista, around 250 km at 05:50 UT (red arrow), which presents a highly atypical altitude formation compared with previous reports on spread Es occurrences (Moro et al., 2025). At the same time, a nocturnal E-region seems to form at altitudes below 150 km, suggesting the presence of additional ionization, as mentioned in Resende et al. (2024). These observations indicate that particle precipitation at different energy levels acts on the ionosphere and likely contributes to the formation of such unusual layers.

The layer observed at approximately 250 km exhibits unique characteristics that deviate significantly from those expected of an E layer. Although this layer exhibits morphological features similar to those of an Es layer, it forms at altitudes within the F region rather than within the typical E-region altitude range where Es layers are usually detected. Therefore, it may be interpreted as an intermediate layer. These characteristics indicate that the mechanism responsible for the formation of this layer may not fully correspond to conventional Es formation mechanisms, and uncertainties regarding the true nature of this layer cannot be ruled out.

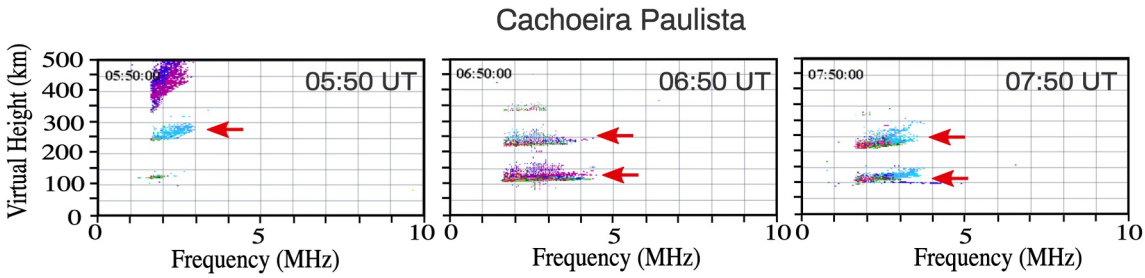

Figure 1. Ionograms recorded at Cachoeira Paulista at three different times (05:50 UT, 06:50 UT, and 07:50 UT) on 18 July 2017, showing the presence of Es-a layers at high altitudes, highlighted by red arrows.

Additionally, the layer near ∼250 km exhibits a smooth downward motion while remaining embedded within the reflection of a lower layer. At 06:50 UT, an E layer is observed at altitudes of approximately 120–130 km, along with an additional Es layer and/or a secondary reflection at 240–250 km. This configuration persists until about 07:50 UT, when two distinct traces become evident, resembling two spreading layers in addition to the secondary reflection trace. This behavior suggests the involvement of physical mechanisms beyond wind shear, as spreading E signatures are commonly associated with particle precipitation or plasma irregularities.

To clarify this behavior, Figure SI4 presents a sequence of ionograms from 04:50 to 07:40 UT. The atypical E layer first appears at ∼05:40 UT at virtual heights above 250 km, with echoes arriving mainly from the north-northeast (NNE; blue). A weaker lower layer, identified as an Esf layer, is also observed near 100 km, with a maximum frequency of ∼2 MHz and echoes arriving from a different direction (green). This directional difference is essential for distinguishing the two layers, since multiple reflections should preserve the direction of the primary trace.

Although a multiple reflections of the lower layer appear in the background of the upper trace, the high-altitude atypical layer exhibits a distinct direction and temporal evolution. The discrete echoes associated with this newly developing layer become progressively stronger over the following 10 min, indicating the formation and intensification of an additional ionospheric layer. Meanwhile, spread-F signatures associated with F-region plasma irregularities remain present at distinctly higher virtual heights. By 06:10 UT, the atypical layer near 250 km continued to intensify, whereas the higher-altitude spread-F signatures began to weaken and disappeared.

Between 06:00 and 06:10 UT, the directional separation is particularly clear. After 06:20 UT, the lower E layer intensifies, while the upper layer gradually weakens and becomes less evident by ∼06:50 UT. These independent variations support the interpretation that an additional high-altitude layer was present, rather than all traces being produced solely by multiple reflections. Therefore, the diffuse or spread trace observed at certain times may indicate additional ionization, possibly associated with energetic-particle precipitation.

At approximately 07:10 UT, this trace reappears at an altitude of ∼150 km. Owing to the limited temporal resolution of the Digisonde measurements, it is not possible to determine whether the trace observed at 150 km represents the formation of a new layer or a rapid downward displacement of the pre-existing atypical intermediate layer. The latter interpretation, commonly associated with disturbed electric fields, is considered plausible given that this layer was initially located at altitudes where electric field effects are significant (Santos et al., 2021).

Thus, as previously mentioned, these observations suggest that multiple factors influence this intermediate layer development, involving not only the formation mechanisms but also background oscillations that help sustain them, as proposed by Resende et al. (2023). Such oscillations are typically generated by short-duration atmospheric waves or winds in low-latitude regions, as well as by electric fields at higher latitudes. Furthermore, the rapid descent of the uncommon layer can only be explained by the presence of a disturbed electric field.

The role of electric fields in the E layer dynamics remains under discussion. While Resende et al. (2021) argued that electric fields are not essential for Es layer formation, Resende et al. (2024) emphasized their role in driving vertical plasma dynamics rather than in generating the layers themselves. Considering that intermediate layers can be influenced by disturbed electric fields (Dos Santos et al., 2019), it is reasonable to infer that electric fields may have played an important role in the subsequent downward motion of this layer.

21699402, 2026, 8, Downloaded from https://agupubs.onlinelibrary.wiley.com/doi/10.1029/2026JA035200 by Center For Space Science And Applied Research, CAS, Wiley Online Library on [19/11/2026]. See the Terms and Conditions (https://onlinelibrary.wiley.com/terms-and-conditions) on Wiley Online Library for rules of use; OA articles are governed by the applicable Creative Commons License

21699402, 2026, 8, Downloaded from https://agupubs.onlinelibrary.wiley.com/doi/10.1029/2026JA035200 by Center For Space Science And Applied Research, CAS, Wiley Online Library on [19/11/2026]. See the Terms and Conditions (https://onlinelibrary.wiley.com/terms-and-conditions) on Wiley Online Library for rules of use; OA articles are governed by the applicable Creative Commons License

Additionally, the occurrence of Es layers at low latitudes is controlled by several mechanisms, and over the SAMA region, there may be an additional contribution from particle precipitation. Recently, several studies have investigated the formation of auroral-type Es layers over the SAMA, particularly Resende et al. (2024, 2025), Moro et al. (2025), and references therein. During geomagnetic storms, hiss waves can be observed within the plasmasphere (Chen et al., 2025; Ding et al., 2025; Lu et al., 2025; Yi et al., 2024), where they interact resonantly with bouncing electrons at low pitch angles, causing pitch-angle scattering and subsequent precipitation over the SAMA region (Da Silva et al., 2023a, 2025). This wave-particle interaction can be further enhanced during extreme geomagnetic storms. For example, during the 10 May 2024 storm, similar mechanisms were observed to contribute to the formation of auroral-type Es layers in the equatorial region over the SAMA (Resende et al., 2024) and in other regions (Qiu & Liu, 2025; Qiu et al., 2025).

Auroral-type E layers are commonly observed around 100–150 km altitude. However, since the energy peak of precipitating electrons is controlled by wave-particle interactions mediated by whistler-mode waves (Paulikas, 1975), the deposition altitude increases as the electron energy decreases (see, e.g., Abdu et al., 1973; Table A1). Therefore, a broad energy range of precipitating electrons may be responsible for the simultaneous observation of auroral-type signatures at multiple altitudes. Finally, we observed a spread trace at high altitudes, suggesting that intermediate layers may be influenced by energetic particles.

3.2. Overview of the Geomagnetic Storm and Magnetospheric Conditions

The complete scenario at the Earth's bow shock nose is analyzed using upstream solar wind measurements from the ACE satellite between July 16 and 18, 2017. This analysis considers the period before and during the detection of the atypical Es-like layer in the center of the SAMA region, as shown in Figure SI2 of Supporting Information S1. An Interplanetary Coronal Mass Ejection (ICME) associated with an interplanetary shock (first vertical line) impacted the Earth's magnetosphere at 05:14 UT on July 16, causing a sudden impulse (SI), more intense than ∼70 nT, as indicated by positive SYM-H values (panel e). During the influence of this shock (first vertical line), the solar wind velocity (panel b) and proton density (panel c) reached values above 450 km/s and 50 particles/cm^3, respectively. The southward component of the interplanetary magnetic field (IMF Bz), shown in panel (a), exhibits a positive enhancement during the shock, followed by negative values that reached −10 nT right after the SI. This moderate geomagnetic storm (SYM-H reached −50 nT) reached the main phase peak about 4 hr following the SI. The AE index (panel d) reached maximum values above 1,700 nT during the main phase of the storm, and exceeded 500 nT during the interplanetary shock, remaining at elevated levels throughout the recovery phase. This behavior of the AE index (panel d) suggests the occurrence of substorms for more than 60 hr following the shock arrival. The recovery phase of this storm was considerably long, with a gradual decrease in substorm activity beginning early on July 17 and continuing until the end of that day (panel e), when AE values dropped below 300 nT. At the time of detection of the atypical Es layer in the center of the SAMA region (05:50 UT–second vertical line), the interplanetary parameters were considerably low, suggesting a period of reduced substorm activity, with the AE index below 250 nT.

Although this magnetic storm was moderate, the magnetosphere exhibited uncommon behavior that may have led to atmospheric impacts. To investigate this context, the magnetospheric conditions were modeled (Figure 2) using a three-dimensional MHD approach, as described in the Data and Methodology section. The initial conditions are defined by the solar wind plasma parameters (Figures SI2 and SI3 in Supporting Information S1) measured by instruments onboard the ACE satellite. The modeled period spans from 04:00 to 07:00 UT on 18 July 2017, encompassing the interval during which the atypical Es layer was detected at an unusually high altitude, near 250 km, at 05:50 UT (as shown in the next section). Two simulations were performed using the same initial condition: one with a fixed dipole configuration (no tilt) and another including dipole tilt according to the time of year, in order to examine the large asymmetry in the dipole inclination associated with season effects. These simulations in Figure 2 consider the time when satellite Van Allen Probe B passed over the SAMA region (see Figure SI1 in Supporting Information S1) a few minutes before the IMF Bz component changed its orientation southward, as shown in Figure SI2 of Supporting Information S1 (external black line - Supporting Information S1). This MHD model is used to investigate the response of the global magnetospheric processes, as well as inner magnetosphere dynamics that may influence the ionized atmosphere over the SAMA region.

The asymmetry observed during the study period, associated with dipole inclination (right panel in Figure 2), can trigger processes capable of producing a pronounced greater illumination intensity in the Northern Hemisphere

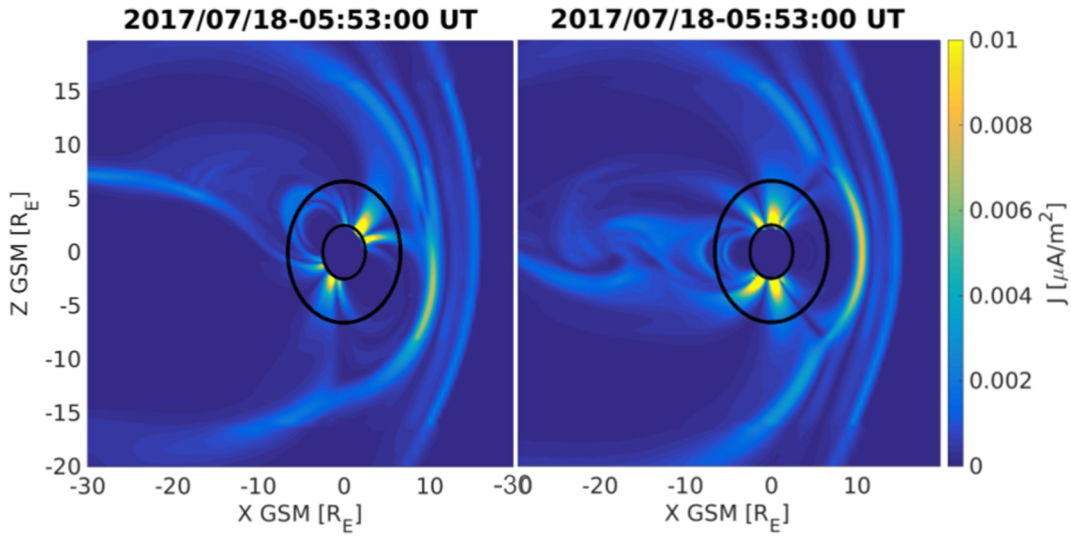

Figure 2. Modeled current density (J) in the meridional plane ($y = 0$) on 18 July 2017, starting at 04:00 UT, with a total duration of 3 hr (Left panel–without dipole tilt): Modeled current density (J) at 05:53 UT without considering the geomagnetic field inclination. (Right panel–with dipole inclination): Modeled current density (J) at 05:53 UT, including the effects of the geomagnetic field inclination. The black circles denote the model's inner boundary, while the outermost circles correspond to the geosynchronous orbit.

than in the Southern Hemisphere, leading to significant changes in the ionosphere, thermosphere, and upper atmosphere, not only at high latitudes but also at low latitudes. The dipole tilt modifies magnetospheric convection driven by magnetic reconnection, which occurs at the Earth's magnetopause and in the magnetotail. During periods of low tilt, the plasma sheet is located near $z = 0$ in GSM coordinates, whereas for larger tilts it shifts to positive z values, altering particle drift paths and natural circulation of magnetospheric plasma. The energetic particle precipitation in the auroral regions is influenced by both dipole tilt and the orientation of the IMF Bz component (Cnossen & Richmond, 2012; Liu et al., 2009). Consequently, the macroscopic changes driven by the dipole tilt, particularly the modulation of magnetospheric convection and the plasma sheet location, directly control the injection of particle populations into the inner magnetosphere. Since the temperature anisotropy of the injected electrons can provide free energy for wave generation, the dipole tilt may ultimately influence plasma wave activity within the inner radiation belt. As discussed in Section 3.2.1, this altered macroscopic topology is a key factor for understanding the atypical behavior of hiss and magnetosonic waves observed by the Van Allen Probes, which, in turn, modulated the altitude of particle precipitation over the SAMA.

3.2.1. Inner Radiation Belt Conditions

The dynamics of the inner radiation belt are analyzed using Van Allen probe B measurements obtained during the formation of a spread Es layer detected near 250 km at 05:50 UT on 18 July 2017 (Figure 3). During this perigee passage, the spacecraft traversed South America, with its magnetic footprint crossing the central region of the SAMA, as shown in Figure SI1 of Supporting Information S1.

Figure 3 shows the Power Spectral Density (PSD) of the magnetic field (top panel), and the electron flux decreases of the energy levels between 10 eV and 50 keV (bottom panel) from 03:00 UT to 08:00 UT, including the inner belt region. Plasmaspheric hiss and magnetosonic (MS) waves are detected in the inner radiation belt from 05:52 UT, as indicated by the corresponding ellipticity (Figure SI5 in Supporting Information S1–medium panel) and planarity (Figure SI5 in Supporting Information S1–bottom panel) values (see Da Silva et al., 2022, 2023a; Li et al., 2019). An atypical feature is observed in the inner radiation belt from 05:52 UT onward, specifically, the absence of hiss and MS waves activity in the 40–200 Hz frequency range (power spectral density $\sim 10^{-8}$ nT^2/Hz). This behavior may inhibit the occurrence of resonant waves-particle interactions within certain energy levels of the inner radiation belt, suggesting a possible change in the altitude of the ionization rate integrated peak, which is typically located between 100 and 150 km (Da Silva et al., 2022, 2023a). Consequently, the ionization peak may

21699402, 2026, 8, Downloaded from https://agupubs.onlinelibrary.wiley.com/doi/10.1029/2026JA035200 by Center For Space Science And Applied Research, CAS, Wiley Online Library on [19/11/2026]. See the Terms and Conditions (https://onlinelibrary.wiley.com/terms-and-conditions) on Wiley Online Library for rules of use; OA articles are governed by the applicable Creative Commons License

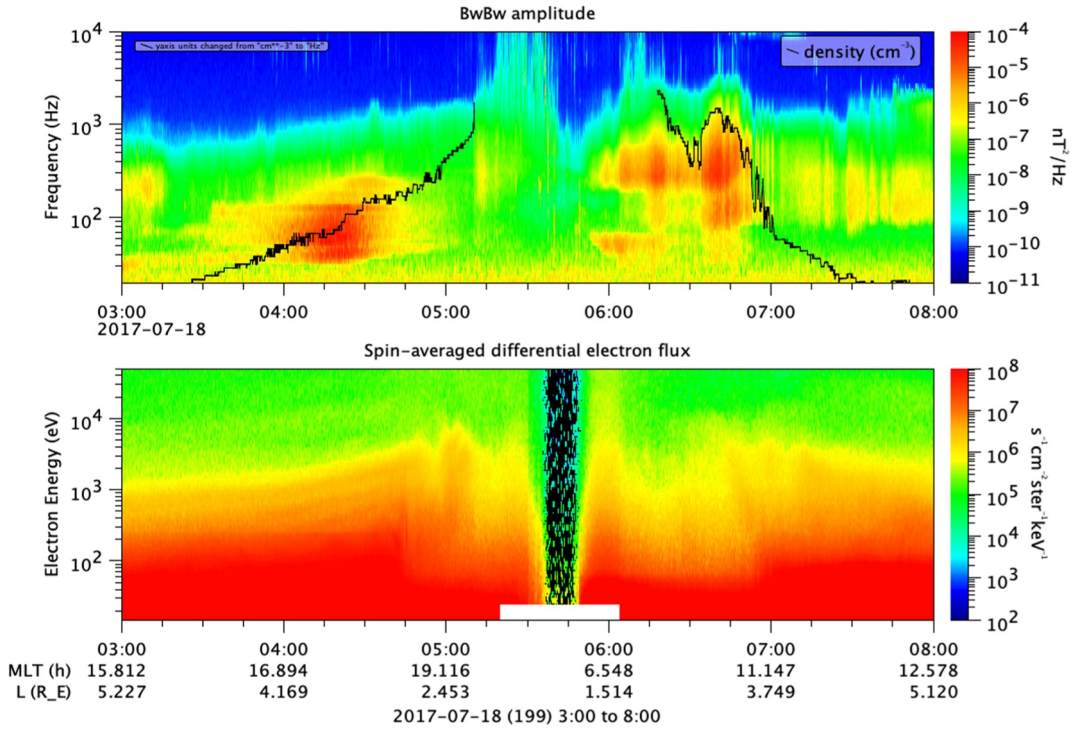

Figure 3. (Top panel) The frequency-time spectrogram of the magnetic field; (Bottom panel) The electron flux (eV). The black line represents the total electron density. The data are obtained from EMFISIS and HOPE instruments onboard the Van Allen Probe B.

occur at higher altitudes, as no plasma waves are available to efficiently interact with electrons in the tens of keV energy range.

This behavior indicates that the dynamics of the inner radiation belt differ from those typically observed during intense geomagnetic storms (Da Silva et al., 2022; Resende et al., 2024). These results suggest that processes in both the external and internal magnetosphere contribute to the formation of spread-type layers at high altitudes, with particle precipitation playing a key role in this occurrence.

Two main mechanisms have been proposed to explain the entry of energetic particles into the atmosphere over the SAMA. The first is a collisional process associated with Coulomb scattering, through which low-energy particles from the inner radiation belt can enter the loss cone and reach mirror points near 100 km altitude (Abdu et al., 1981, 2005). This process occurs continuously and has been used to explain enhanced ionization under quiet conditions, as discussed by Abdu et al. (2005), as well as the enhanced nocturnal E region observed during the main phase of geomagnetic storms, as shown by Resende et al. (2024).

The second mechanism involves the interaction between MS and hiss types magnetospheric waves and electrons, particularly low-energy electrons ranging from approximately 0.5 keV to tens of keV. This interaction can cause pitch-angle scattering and lead to the violation of the first and/or second adiabatic invariant, allowing particles to precipitate into the atmosphere (Da Silva et al., 2022). This mechanism has been proposed to explain the occurrence of spread Es traces in ionograms over the SAMA region, as previously reported in the literature (Batista & Abdu, 1977; Da Silva et al., 2022; Moro et al., 2022).

When this spread trace occurs near 100 km altitude, it is commonly referred to as an auroral-like trace or Esa layer, and it is mainly observed during the recovery phase of geomagnetic storms. Therefore, this atypical spread trace is generally interpreted as an indication of particle precipitation. To evaluate whether auroral-like traces occurred during this magnetic storm, we also examined the subsequent days. Diffuse or spread-type Es traces were observed near 100 km in the ionograms recorded between 20:40 and 21:10 UT on 21 July (Figure SI7), suggesting that energetic-particle precipitation may have affected the lower ionosphere during these intervals. However, similar auroral-type Es signatures and their association with particle precipitation have already been

21699402, 2026, 8, Downloaded from https://agupubs.onlinelibrary.wiley.com/doi/10.1029/2026JA035200 by Center For Space Science And Applied Research, CAS, Wiley Online Library on [19/11/2026]. See the Terms and Conditions (https://onlinelibrary.wiley.com/terms-and-conditions) on Wiley Online Library for rules of use; OA articles are governed by the applicable Creative Commons License

21699402, 2026, 8, Downloaded from https://agupubs.onlinelibrary.wiley.com/doi/10.1029/2026JA035200 by Center For Space Science And Applied Research, CAS, Wiley Online Library on [19/11/2026]. See the Terms and Conditions (https://onlinelibrary.wiley.com/terms-and-conditions) on Wiley Online Library for rules of use; OA articles are governed by the applicable Creative Commons License

extensively investigated in previous studies (Da Silva et al., 2023a; Moro et al., 2022). Therefore, a detailed analysis of these post-storm occurrences is beyond the scope of the present work.

Nevertheless, in the present study, we observed a similar spread trace, but at higher altitudes, indicating that particle precipitation may also affect different altitude regions. For this reason, we refer to this feature as an atypical intermediate layer. It is important to emphasize that the occurrence of this spread layer likely requires a background mechanism capable of supporting the formation of intermediate or Es-like layers, such as vertical wind shear. In addition, as discussed by Resende et al. (2023), the power of hiss waves is essential for the formation of atypical layers. Therefore, if one of the necessary conditions is absent, the layer may not form. In this context, magnetospheric wave activity may increase both the probability and intensity of spread-layer formation over the SAMA region.

3.3. Ionization Rate Modeled

The atypical inner radiation belt dynamic conditions, close to 05:50 UT analyzed before, suggested that the electrons from 1 keV are trapped, which means that the amount of electron precipitation in the altitudes 90–150 km is considerably reduced when compared with the typical inner belt conditions as observed in Da Silva et al. (2022, 2023a), Resende et al. (2024) and Moro et al. (2025). Therefore, the estimation of the atmospheric ionization rate over the center of the SAMA region at 05:50 UT on July 18 is necessary to confirm that the atypical inner belt conditions have triggered of the physical processes responsible for the low-energy electron precipitation (below 1 keV) into the atmosphere during the generation of the atypical sporadic Es layer detected in Cachoeira Paulista. The empirical model to estimate the ionization rate at Cachoeira Paulista considers the parameterization of ionization in the atmosphere driven by the isotropically precipitating monoenergetic electrons (100 eV–1 MeV) (Fang et al., 2010). This model assumes that the incident particles given by differential number flux ($cm^{-2}\ s^{-2}\ keV^{-1}$) have a Maxwellian distribution. This distribution was derived through forward modeling to estimate the electron energy distribution required to reproduce the ionogram signature (Figure 4). The differential number flux was fitted using Equation 1, following Fang et al. (2010, their Equation 6), where E_0 is the characteristic energy, ranging from 10 to 27 eV in our fit, and Q_0 is the total energy flux. This parameterization, originally proposed by Fang et al. (2010) and further discussed by Da Silva et al. (2022), is based on satellite observations.

$$\Phi_M(E) = \frac{Q_0}{2E_0^3} E \exp\left(-\frac{E}{E_0}\right), \tag{1}$$

The low characteristic energy is consistent with the observed suppression of wave activity. Since hiss and magnetosonic waves were absent in the 40–200 Hz frequency range (Figure 3), resonant scattering of tens-of-keV electrons into the loss cone was likely suppressed. Consequently, the remaining precipitation was dominated by sub-keV electrons entering the loss cone through Coulomb scattering and geometric mirror-point effects at SAMA altitudes.

We note that the parameterization proposed by Fang et al. (2010) is formally valid for energies $E \geq 100$ eV. Therefore, the ionization profile presented here should be interpreted as an illustration of the altitude range expected for the sub-keV precipitation inferred from HOPE observations. This interpretation is bounded at the lower end by the 100 eV result reported by Fang et al. (2010, their Figure 2b), which places the ionization peak at approximately 220–240 km under disturbed conditions.

The ionization rate over Cachoeira Paulista at 05:50 UT on July 18, shown in Figure 4 (left panel), indicates very low-energy levels (10–27 eV), which, as expected, leads to a maximum peak in the integrated ionization rate between 250 and 300 km altitude ($\sim 10^5\ cm^{-3}\ s^{-1}$), as shown in Figure 4 (middle panel). The critical frequency (foE), derived from the modeled electron density profile using the plasma frequency relation (Nikolaeva et al. (2021, their Equation 6), foE (MHz) = (Ne [m^{-3}]/1.24 × 10^{10})^(1/2), where Ne is the electron number density in m^{-3}, is shown in Figure 4 (red line in right panel) and is observed at altitudes above 180 km. Interestingly, the vertical profile of this critical frequency coincides with the height base of the atypical sporadic layer detected over Cachoeira Paulista at the same time, as shown in Figure 4 (red line in right panel). This result is consistent with Da Silva et al. (2022, 2023a), who reported that the height base of the sporadic Es layer coincides with the modeled critical frequencies. Moreover, this finding suggests that this atypical sporadic Es layer is

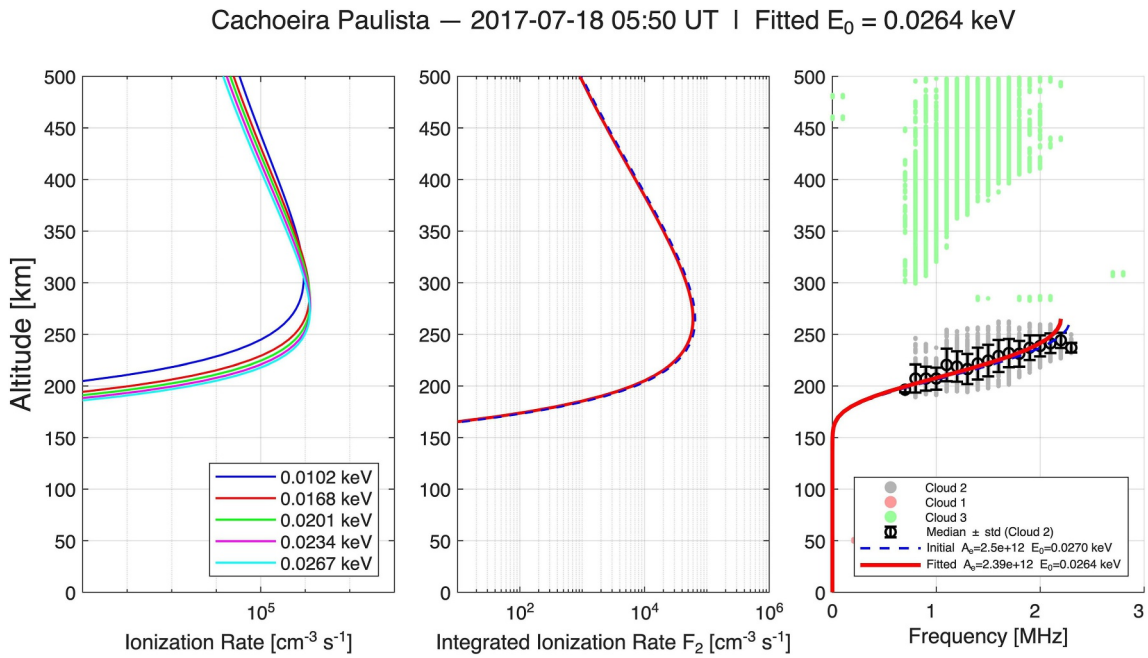

Figure 4. Ionization rate altitude profiles (left panel), ionization rate altitude integrated (middle panel), and critical modeled frequency altitude (right panel) estimated over Cachoeira Paulista at 5:50 UT on 18 July 2017. The ionization rate is obtained from an empirical model (Fang et al., 2010) considering the total incident energy of electrons presented in Figure SI6.

formed at altitudes close to 250 km associated with enhanced precipitation of very low-energy electrons (<1 keV), whose flux exceeds the quantity of low-energy electrons (tens of keV). This behavior is attributed to the peculiar dynamics of the inner radiation belt, particularly the absence of hiss and MS waves activity in the 40–200 Hz frequency range. Consequently, electron precipitation is characterized by predominantly very low energies and significantly enhanced fluxes.

Although the formation of sporadic Es layers associated with the presence of EPP over the SAMA region has been widely investigated by the scientific Brazilian community (e.g., Da Silva et al., 2025; Moro et al., 2025; Resende et al., 2024), the physical processes responsible for their intrinsic characteristics are still not fully understood. Here, we present strong evidence that particle precipitation played a key role in the formation of the spread-type E layer.

Finally, we also examined ionograms recorded at Santa Maria (29.7°S, 53.8°W; dip: −37°), located near the central region of the SAMA, during intervals close to those analyzed over Cachoeira Paulista. A weak atypical layer was identified at virtual heights above ∼150 km, with echoes arriving from a direction similar to those observed over Cachoeira Paulista, suggesting a coherent reflecting structure (Figure SI8 in Supporting Information S1). The occurrence of elevated atypical layers at both stations during nearly the same disturbed interval supports the interpretation that this feature represents an additional intermediate layer, likely formed by enhanced ionization potentially associated with energetic-particle precipitation, together with a favorable background dynamical mechanism such as vertical wind shear.

3.4. Atmospheric Evidence of EPP Over the SAMA Region

The atmospheric composition over the SAMA region is considerably affected by EPP during geomagnetic storms (e.g., Da Silva et al., 2022, 2023a, 2025; Moro et al., 2025), since electrons with different energy levels deposit their energy at different altitudes according to their stopping depths in the atmosphere. Although the present study focuses on a relatively short interval associated with the formation of an atypical spread Es layer observed on 18 July at 5:50 UT, investigating atmospheric composition changes at other altitudes throughout 18 July can provide additional evidence of EPP over the SAMA region.

Therefore, to assess whether EPP affected the atmosphere at altitude beyond those associated with the observed Es layer, we employed additional satellite observations to indirectly evaluate mesospheric ozone variability.

21699402, 2026, 8, Downloaded from https://agupubs.onlinelibrary.wiley.com/doi/10.1029/2026JA035200 by Center For Space Science And Applied Research, CAS, Wiley Online Library on [19/11/2026]. See the Terms and Conditions (https://onlinelibrary.wiley.com/terms-and-conditions) on Wiley Online Library for rules of use; OA articles are governed by the applicable Creative Commons License

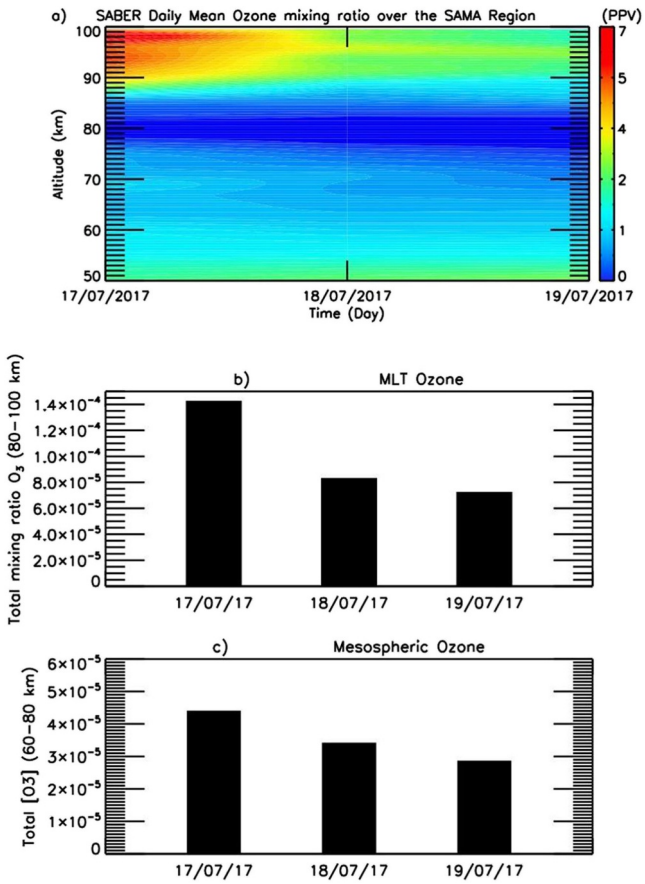

Figure 5. (a) Daily average ozone mixing ratio 9.6 μm over the SAMA region; (b) integrated column of ozone in the MLT region, from 80 to 100 km; and (c) integrated column of mesospheric ozone, between 60 and 80 km. The SAMA region was considered using a grid of 10° on latitude and 20° on longitude, from 30°S to 20°S, and 40°W to 60°W. The data was obtained from TIMED/SABER.

Specifically, ozone mixing ratio measurements from the TIMED/SABER instrument were analyzed over the SAMA region during 17–18 July 2017. However, it is important to note that ozone depletion in the mesosphere develops throughout the recovery phase of a geomagnetic storm, primarily due to the time required to produce HOx and NOx species and subsequent catalytic processes responsible for ozone destruction (e.g., Sinnhuber et al., 2012; Vampola & Gorney, 1983).

The analysis encompassed three consecutive days, including one day before and one day following the E layer event. The TIMED orbits relevant to this study are listed in Table A1. Within the defined spatial grid and temporal window, 16 profiles were obtained, and the corresponding event characteristics are also summarized in Table A1. Daily averaged profiles were subsequently constructed and are presented in Figure 5 (panel a) as altitude-color contour plots from 50 to 100 km. Owing to the slow precession orbit of TIMED, the measurements were acquired under nearly identical local time conditions, thereby minimizing day-to-day variability.

The ozone mixing ratio exhibits a decrease from ∼50 to 80 km, followed by an increase associated with the secondary ozone maximum near 95 km, as shown in Figure 5 (panel a). A pronounced depletion in this secondary ozone maximum is evident after July 17, which coincides with the final of the storm recovery phase, including the period of atypical Es layer detection. To better characterize this depletion and assess the potential role of EPP in modulating ozone over the SAMA, column-integrated values were calculated from the daily mean profiles between 60 and 80 km (mesospheric ozone), and between 80 and 100 km (MLT region), as shown in Figure 5 (panels b and c, respectively). The results indicate an abrupt reduction in the integrated ozone mixing ratio from July 17 to 18, with decreases of approximately 22% in the mesosphere and 58% in the MLT region. This means that the atmosphere over the SAMA region exhibits behavior analogous to that of the auroral regions during geomagnetic storm conditions (Newnham et al., 2020; Tartaglione et al., 2020). In such circumstances, EPP into the neutral atmosphere leads to enhanced production of odd nitrogen (NOx) and odd hydrogen (HOx), which in turn catalytically drive ozone depletion (e.g., Da Silva et al., 2025; Frolov & Troitsky, 2023). It is important to emphasize that this pronounced ozone depletion over the SAMA region occurred under the influence of a moderate geomagnetic storm and is substantially greater than the depletion reported by Da Silva et al. (2025), which was observed during an extreme geomagnetic storm. Therefore, this behavior provides evidence for the action of EEP, and the relationship between EEP and magnetic storm intensity is not yet fully understood and will be examined in future studies.

4. Concluding Remarks

We present an analysis of atypical E layer behavior observed during the recovery phase of a moderate geomagnetic storm on 18 July 2017 over the SAMA. The observations reveal the occurrence of unusual auroral-like Esa layers at unusually high altitudes. By combining ground-based ionospheric measurements with space-borne observations, we investigated the coupled processes responsible for the formation of these anomalous structures.

Ionograms show a spread E trace near ∼250 km at 05:50 UT, coincident with the development of an E-region layer initiating below ∼150 km. This simultaneous occurrence suggests the presence of additional ionization sources acting across multiple ionospheric altitudes in regions under the influence of the SAMA. These features are consistent with particle precipitation spanning a range of energies, contributing to the formation and modification of E layers.

A plausible mechanism to explain the formation of the anomalous Es layer at ∼ 250 km and E layer formation near 150 km involves particle precipitation at different energy ranges, which leads to ionization being deposited at

21699402, 2026, 8, Downloaded from https://agupubs.onlinelibrary.wiley.com/doi/10.1029/2026JA035200 by Center For Space Science And Applied Research, CAS, Wiley Online Library on [19/11/2026]. See the Terms and Conditions (https://onlinelibrary.wiley.com/terms-and-conditions) on Wiley Online Library for rules of use; OA articles are governed by the applicable Creative Commons License

21699402, 2026, 8, Downloaded from https://agupubs.onlinelibrary.wiley.com/doi/10.1029/2026JA035200 by Center For Space Science And Applied Research, CAS, Wiley Online Library on [19/11/2026]. See the Terms and Conditions (https://onlinelibrary.wiley.com/terms-and-conditions) on Wiley Online Library for rules of use; OA articles are governed by the applicable Creative Commons License

distinct altitudes. With respect to the Es layer, which exhibits characteristics similar to the Esa layer in terms of its spread morphology, its formation may not be fully explained by conventional Es generation mechanisms. The available evidence of atypical conditions in both the internal and external magnetosphere helps elucidate the physical processes responsible for the development of this highly unusual layer.

An additional atypical feature is identified in the inner radiation belt starting at ∼05:52 UT, characterized by the absence of plasmaspheric hiss and magnetosonic (MS) wave activity in the 40–200 Hz frequency range. This suppression of wave activity may inhibit resonant wave-particle interactions for specific electron energy populations, thereby altering the altitude distribution of ionization. In particular, the altitude of the integrated ionization rate peak, typically located between 100 and 150 km, may be displaced upward due to the lack of plasma waves capable of scattering electrons in the tens of keV energy range.

Modeling results support this interpretation, indicating that the atypical Es layer formed near ∼250 km is primarily driven by enhanced precipitation of very low-energy electrons, whose flux exceeds that of higher-energy (tens of keV) electrons. This behavior appears to be linked to the unusual dynamics of the inner radiation belt during the event, including the absence of hiss and MS waves, which favored strong precipitation of low-energy electrons.

To further assess the role of energetic particle precipitation, we indirectly examined mesospheric ozone behavior over the SAMA region. Ozone mixing ratio measurements from the TIMED/SABER instrument reveal a decrease between 50 and 80 km, followed by an increase associated with the secondary ozone maximum near ∼95 km. Notably, a pronounced depletion of this secondary ozone maximum was observed after 17 July 2017, coincident with the late recovery phase of the storm and the period during which the atypical Es layers were detected. This behavior is indicative of auroral-like atmospheric responses, which enhance the production of odd nitrogen (NOx) and odd hydrogen (HOx), leading to catalytic ozone depletion. Importantly, this significant ozone reduction over the SAMA occurred during a geomagnetic storm of only moderate intensity, highlighting the region's heightened sensitivity to particle precipitation.

Appendix A

The ozone data used in this study were obtained from the Sounding of the Atmosphere using Broadband Emission Radiometry (SABER) instrument onboard the Thermosphere, Ionosphere, Mesosphere, Energetics, and Dynamics (TIMED) satellite (Russell et al., 1999). The orbital information of the TIMED satellite for the events analyzed during the study period, corresponding to the ozone retrievals from SABER, is summarized in Table A1.

Table A1
TIMED Orbit Information for Ozone Retrievals From SABER Instrument

Orbit	Event	Date	Time	Latitude	Longitude	Solar zenith angle
84593	93	17/07/2017	01:31:58	−27.7304	314.574	157.264
84593	94	17/07/2017	01:33:08	−23.7342	314.839	158.237
84593	95	17/07/2017	01:33:51	−21.3349	315.045	158.555
84608	90	18/07/2017	01:44:27	−27.1362	308.523	154.724
84608	91	18/07/2017	01:45:09	−24.7433	308.683	155.262
84608	92	18/07/2017	01:46:20	−20.763	309.023	155.778
84614	52	18/07/2017	10:48:24	−23.5899	316.348	75.8793
84614	53	18/07/2017	10:49:06	−25.9857	316.523	76.8458
84614	54	18/07/2017	10:50:17	−29.9975	316.735	78.5935
84623	91	19/07/2017	01:56:05	−29.4637	302.321	151.4
84623	92	19/07/2017	01:57:14	−25.5583	302.547	152.335
84623	93	19/07/2017	01:58:00	−22.9241	302.75	152.751
84629	52	19/07/2017	10:59:41	−20.0679	309.96	76.9534
84629	53	19/07/2017	11:00:23	−22.4718	310.175	77.7791
84629	54	19/07/2017	11:01:34	−26.4607	310.468	79.2684
84629	55	19/07/2017	11:02:19	−29.0253	310.603	80.3078

Conflict of Interest

The authors declare no conflicts of interest relevant to this study.

Availability Statement

The data used in this article are available: HOPE instrument data: https://cdaweb.gsfc.nasa.gov/pub/data/rbsp/. EMFISIS instrument data: https://emfisis.physics.uiowa.edu/Flight/. TIMED/SABER: https://saber.gats-inc.com. EMBRACE-Ionosonde: https://www2.inpe.br/climaespacial/portal/. ACE satellite data: http://www.srl.caltech.edu/ACE/ASC/DATA/browse-data/. AE and SYM-H indices: https://omniweb.gsfc.nasa.gov/form/omni_min.html.

Acknowledgments
We thank the Brazilian Ministry of Science, Technology, and Innovation (MCTI), the Brazilian Space Agency (AEB), the Space Weather Division (DICEP), and the National Institute for Space Research (INPE). L.A.S., L.C.A.R., P.R.J, A.S., J.M and V.F.A. are grateful for financial support from China-Brazil Joint Laboratory for Space Weather (CBJLSW), State Key Laboratory for Space Weather, National Space Science Center, Chinese Academy of Sciences, National Space Science Center (NSSC), and the Chinese Academy of Science (CAS). This work was supported by the International Partnership Program of the Chinese Academy of Sciences (Grants 119GJHZ2024027MI). L.E.V. thanks CNPq/MCTI (Grant 307404/2016-1), TED-004/2020-AEB, and PO-20VB.0009. L.R.A. thanks to CNPq/MCTI (Grant 301476/2018-7). L.A.S. thanks to CNPq/MCTI (Grant 312906/2023-4) and FAPESP (Grant 2025/25881-7). J.M. thanks the National Council for Scientific and Technological Development (CNPq) Grant 305041/2024-0. J.P.M. thanks CNPq/MCTI (Grant 447404/2024-5). C. M.D. thanks to CNPq/MCTI (Grant 302675/2021-3). L.E.V. thanks CNPq/MCTI (Grant 309735/2025-4), FAPESP (2026/06386-8), TED-004/2020-AEB, and PO-20VB.0009. L.R.A. thanks to CNPq/MCTI (Grant 304482/2024-2). L.A.S. thanks to CNPq/MCTI (Grant 312906/2023-4) and FAPESP (Grants 2025/25881-7, 2026/14759-9, 2025/29164-8, 2025/28521-1, 2025/19726-9). L.C.A.R. thanks to CNPq/MCTI (Grant 305657/2026-7) and FAPESP (Grants 2026/06393-4).

References

Abdu, M. A., Ananthakrishnan, S., Coutinho, E. F., Krishnan, B. A., & Reis, E. M. D. S. (1973). Azimuthal drift and precipitation of electrons into the South Atlantic Geomagnetic Anomaly during an SC magnetic storm. *Journal of Geophysical Research*, *78*(25), 5830–5836. https://doi.org/10.1029/JA078i025p05830

Abdu, M. A., Batista, I. S., Carrasco, A. J., & Brum, C. G. M. (2005). South Atlantic magnetic anomaly ionization: A review and a new focus on electrodynamic effects in the equatorial ionosphere. *Journal of Atmospheric and Solar-Terrestrial Physics*, *67*(17–18), 1643–1657. https://doi.org/10.1016/j.jastp.2005.01.014

Abdu, M. A., Batista, I. S., Piazza, L. R., & Massambani, O. (1981). Magnetic storm associated enhanced particle precipitation in the South Atlantic Anomaly evidence from VLF phase measurements. *Journal of Geophysical Research*, *86*(A9), 7533–7542. https://doi.org/10.1029/JA086iA09p07533

Alves, L. R., da Silva, L. A., Deggeroni, V., Marchezi, J. P., Jauer, P. R., Silva, G. B. D., & Sibeck, D. G. (2024). Ultra-relativistic electron flux enhancement under persistent high speed solar wind stream. *Frontiers in Astronomy and Space Sciences*, *11*, 1478489. https://doi.org/10.3389/fspas.2024.1478489

Alves, L. R., Da Silva, L. A., Souza, V. M., Sibeck, D. G., Jauer, P. R., Vieira, L. E. A., et al. (2016). Outer radiation belt dropout dynamics following the arrival of two interplanetary coronal mass ejections. *Geophysical Research Letters*, *43*(3), 978–987. https://doi.org/10.1002/2015GL067066

Andersson, M. E., Verronen, P. T., Rodger, C. J., Clilverd, M. A., & Wang, S. (2014). Longitudinal hotspots in the mesospheric OH variations due to energetic electron precipitation. *Atmospheric Chemistry and Physics*, *14*(2), 1095–1105. https://doi.org/10.5194/acp-14-1095-2014

Batista, I. S., & Abdu, M. A. (1977). Magnetic storm associated delayed sporadic E enhancements in the Brazilian Geomagnetic Anomaly. *Journal of Geophysical Research*, *82*(29), 4777–4783. https://doi.org/10.1029/JA082i029p04777

Bittencourt, J. A. (2004). *Fundamentals of plasma physics* (3rd ed.). Pergamon Press. https://doi.org/10.1007/978-1-4757-4030-1

Borovsky, J. E. (2018). The spatial structure of the oncoming solar wind at Earth and the shortcomings of a solar-wind monitor at L1. *Journal of Atmospheric and Solar-Terrestrial Physics*, *177*, 2–11. https://doi.org/10.1016/j.jastp.2017.03.014

Borovsky, J. E., & Yakymenko, K. (2017). Substorm occurrence rates, substorm recurrence times, and solar wind structure. *Journal of Geophysical Research: Space Physics*, *122*(3), 2973–2998. https://doi.org/10.1002/2016JA023625

Chen, H., Zhu, H., Zhao, Y., Qin, Z., & She, Z. (2025). Hiss waves near the South Atlantic Anomaly in the inner plasmasphere. *Journal of Geophysical Research: Space Physics*, *130*(8), e2025JA034266. https://doi.org/10.1029/2025JA034266

Cnossen, I., & Richmond, A. D. (2012). How changes in the tilt angle of the geomagnetic dipole affect the coupled magnetosphere-ionosphere-thermosphere system. *Journal of Geophysical Research*, *117*(A10), A10317. https://doi.org/10.1029/2012JA018056

Da Silva, L. A., Shi, J., Alves, L. R., Resende, L. C. A., Vieira, L. E. A., Rezende, J. E., et al. (2025). Space weather effects over SAMA during the extreme geomagnetic storm on May 10-11, 2024: Disturbances of the neutral and ionized atmosphere. *Frontiers in Astronomy and Space Sciences*, *12*, 1550635. https://doi.org/10.3389/fspas.2025.1550635

Da Silva, L. A., Shi, J., Alves, L. R., Sibeck, D., Marchezi, J. P., Medeiros, C., et al. (2021b). High-energy electron flux enhancement pattern in the outer radiation belt in response to the Alfvenic fluctuations within high-speed solar wind stream: A statistical analysis. *Journal of Geophysical Research: Space Physics*, *126*(8), e2021JA029363. https://doi.org/10.1029/2021JA029363

Da Silva, L. A., Shi, J., Alves, L. R., Sibeck, D., Souza, V. M., Marchezi, J. P., et al. (2021a). Dynamic mechanisms associated with high-energy electron flux dropout in the Earth's outer radiation belt under the influence of a coronal mass ejection sheath region. *Journal of Geophysical Research: Space Physics*, *126*(1). https://doi.org/10.1029/2020JA028492

Da Silva, L. A., Shi, J., Marchezi, J. P., Agapitov, O. V., Sibeck, D., Alves, L. R., et al. (2023b). High-energy electron flux enhancement pattern in the outer radiation belt in response to the interplanetary coronal mass ejections. *Journal Of Geophysical Research-Space Physics*, *128*(11), 1. https://doi.org/10.1029/2023ja031360

Da Silva, L. A., Shi, J., Resende, L. C. A., Agapitov, O. v., Alves, L. R., Batista, I. S., et al. (2022). The role of the inner radiation belt dynamic in the generation of auroral-type sporadic E-layers over South American Magnetic Anomaly. Front. *Astronomy Space Sci*, *9*, 970308. https://doi.org/10.3389/fspas.2022.970308

Da Silva, L. A., Shi, J., Vieira, L. E., Agapitov, O. v., Resende, L. C. A., Alves, L. R., et al. (2023a). Why can the auroral-type sporadic E layer be detected over the South America Magnetic Anomaly (SAMA) region? An investigation of a case study under the influence of the high-speed solar wind stream. *Frontiers in Astronomy and Space Sciences*, *10*, 1197430. https://doi.org/10.3389/fspas.2023.1197430

Da Silva, L. A., Sibeck, D., Alves, L. R., Souza, V. M., Jauer, P. R., Claudepierre, S. G., et al. (2019). Contribution of ULF wave activity to the global recovery of the outer radiation belt during the passage of a high-speed solar wind stream observed in September 2014. *Journal of Geophysical Research: Space Physics*, *124*(3), 1660–1678. https://doi.org/10.1029/2018JA026184

Ding, X., Wu, Z., He, Z., Yan, Q., Chen, X., Yu, J., & Ma, Y. (2025). The global propagation of hiss waves originating from dynamic plasmaspheric plume. *Geophysical Research Letters*, *52*(24), e2025GL119873. https://doi.org/10.1029/2025GL119873

Dos Santos, Â. M., Batista, I. S., Abdu, M. A., Sobral, J. H. A., Souza, J. R., & Brum, C. G. M. (2019). Climatology of intermediate descending layers (or 150 km echoes) over the equatorial and low-latitude regions of Brazil during the deep solar minimum of 2009. *Annales Geophysicae*, *37*(6), 1005–1024. https://doi.org/10.5194/angeo-37-1005-2019

21699402, 2026, 8, Downloaded from https://agupubs.onlinelibrary.wiley.com/doi/10.1029/2026JA035200 by Center For Space Science And Applied Research, CAS, Wiley Online Library on [19/11/2026]. See the Terms and Conditions (https://onlinelibrary.wiley.com/terms-and-conditions) on Wiley Online Library for rules of use; OA articles are governed by the applicable Creative Commons License

Duderstadt, K. A., Huang, C.-L., Spence, H. E., Smith, S., Blake, J. B., Crew, A. B., et al. (2021). Estimating the impacts ofradiation belt electrons on atmosphericchemistry using FIREBIRD II and VanAllen Probes observations. *Journal of Geophysical Research: Atmospheres*, *126*(7), e2020JD033098. https://doi.org/10.1029/2020JD033098

Echer, E., Gonzalez, W. D., & Tsurutani, B. T. (2008). Interplanetary conditions leading to superintense geomagnetic storms (dst ≤ −250 nT) during solar cycle 23. *Geophys. Res. Lett.*, *35*(6). https://doi.org/10.1029/2007GL031755

Fang, X., Randall, C., Lummerzheim, D., Wang, W., Lu, G., Solomon, S., & Frahm, R. (2010). Parameterization of monoenergetic electron impact ionization. *Geophysical Research Letters*, *37*(22), 22106. https://doi.org/10.1029/2010GL045406

Frolov, V. L., & Troitsky, A. V. (2023). HF-Induced artificial injection of energetic electrons from the earth's radiation belt as a powerful source for modification of ionized and neutral components of the earth's atmosphere. *Atmosphere*, *14*(5), 843. https://doi.org/10.3390/atmos14050843

Funsten, H. O., Skoug, R. M., Guthrie, A. A., et al. (2013). Helium, oxygen, proton, and electron (HOPE) mass spectrometer for the radiation belt storm probes Mission. *Space Science Reviews*, *179*, 423–484.

Gombosi, T. I., Chen, Y., Glocer, A., Huang, Z., Jia, X., Liemohn, M. W., et al. (2021). What sustained multi-disciplinary research can achieve: The space weather modeling framework. *Journal of Space Weather and Space Climate*, *11*, 42. https://doi.org/10.1051/swsc/2021020

Gombosi, T. I., Dezeeuw, D. L., Groth, C. P. T., Powell, K. G., Robert Clauer, C., & Song, P. (2001). From sun to Earth: Multiscale MHD simulations of space weather. In *Space weather* (pp. 169–176). American Geophysical Union (AGU). https://doi.org/10.1029/GM125p0169

Gombosi, T. I., Zeeuw, D. L. D., Powell, K. G., Ridley, A. J., Sokolov, I. V., Stout, Q. F., & Tóth, G. (2003). Adaptive mesh refinement for global magnetohydrodynamic simulation. *Space plasma simulation*, 247–274. https://doi.org/10.1007/3-540-36530-3_12

Gonzalez, W. D., Echer, E., Tsurutani, B. T., Clúa de Gonzalez, A. L., & Dal Lago, A. (2011). Interplanetary origin of intense, superintense and extreme geomagnetic storms. *Space Science Reviews*, *158*(1), 69–89. https://doi.org/10.1007/s11214-010-9715-2

Haldoupis, C. (2011). A tutorial review on sporadic E layers, aeronomy of the Earth's atmosphere-ionosphere. *IAGA Book Series*, *29*(2), 381–394. https://doi.org/10.1007/978-94-007-0326-1_29

Horne, R. B., Lam, M. M., & Green, J. C. (2009). Energetic electron precipitation from the outer radiation belt during geomagnetic storms. *Geophysical Research Letters*, *36*(19), L19104. https://doi.org/10.1029/2009GL040236

Jauer, P. R., Wang, C., Echer, E., Souza, V. M., Da Silva, L. A., Marchezi, J. P., et al. (2022). Global modeling of the inner magnetosphere under the influence of a magnetic cloud associated with an interplanetary coronal mass ejection: Energy conversion and ultra-low frequency wave activity. *Journal of Geophysical Research: Space Physics*, *127*(10), e2022JA030615. https://doi.org/10.1029/2022JA030615

Jauer, P. R., Wang, C., Souza, V., Alves, M., Alves, L., Pádua, M., et al. (2019). A global magnetohydrodynamic simulation study of ultra-lowfrequency wave activity in the inner magnetosphere: Corotating interaction region+ Alfvénic fluctuations. *The Astrophysical Journal*, *886*(1), 59. https://doi.org/10.3847/1538-4357/ab4db5

Kletzing, C. A., Kurth, W. S., Acuna, M., MacDowall, R. J., Torbert, R. B., Averkamp, T., et al. (2013). The electric and magnetic field instrument suite and integrated science (EMFISIS) on RBSP. *Space Science Reviews*, *179*(1–4), 127–181. https://doi.org/10.1007/s11214-013-9993-6

Li, W., Shen, X. C., Ma, Q., Capannolo, L., Shi, R., Redmon, R. J., et al. (2019). Quantification of energetic electron precipitation driven by plume whistler mode waves, plasmaspheric hiss, and exohiss. *Geophysical Research Letters*, *46*(7), 3615–3624. https://doi.org/10.1029/2019GL082095

Li, W., Thorne, R. M., Bortnik, J., Baker, D. N., Reeves, G. D., Kanekal, S. G., et al. (2015). Solar wind conditions leading to efficient radiation belt electron acceleration: A superposed epoch analysis. *Geophysical Research Letters*, *42*(17), 6906–6915. https://doi.org/10.1002/2015GL065342

Liu, L., Zhao, B., Wan, W., Ning, B., Zhang, M.-L., & He, M. (2009). Seasonal variations of the ionospheric electron densities retrieved from constellation observing system for meteorology, ionosphere, and climate mission radio occultation measurements. *Journal of Geophysical Research*, *114*(A2), A02302. https://doi.org/10.1029/2008JA013819

Lu, M., Qin, Z., Zhu, H., Zhao, Y., & Chen, H. (2025). Identification of locally generated plasmaspheric hiss. *Geophysical Research Letters*, *52*(6), e2024GL114051. https://doi.org/10.1029/2024GL114051

Mathews, J. D. (1998). Sporadic E: Current views and recent progress. *Journal of Atmospheric and Terrestrial Physics*, *60*(4), 413–435. https://doi.org/10.1016/S1364-6826(97)00043-6

Mauk, B. H., Fox, N. J., Kanekal, S. G., Kessel, R. L., Sibeck, D. G., & Ukhorskiy, A. (2013). Science objectives and rationale for the radiation belt storm probes mission. *Space Science Reviews*, *179*(1–4), 3–27. https://doi.org/10.1007/s11214-012-9908-y

Moro, J., Xu, J., Bageston, J. V., Da Silva, L. A., Resende, L. C. A., De Nardin, C. M., et al. (2025). Study of height-spread sporadic-E layers observed in the South American Magnetic Anomaly. *Frontiers in Astronomy and Space Sciences*, *12*, 1535186. https://doi.org/10.3389/fspas.2025.1535186

Moro, J., Xu, J., Denardini, C. M., Resende, L. C. A., da Silva, L. A., Chen, S. S., et al. (2022). Different sporadic-E (Es) layer types development during the August 2018 geomagnetic storm: Evidence of auroral type (Es a) over the SAMA region. *Journal of Geophysical Research: Space Physics*, *127*(2), e2021JA029701. https://doi.org/10.1029/2021JA029701

Murase, K., Kataoka, R., Tanaka, Y., Nishiyama, T., Hashimoto, T., & Sato, K. (2025). Atmospheric ionization caused byEMIC-wave driven energetic electronprecipitation at auroral latitude. *Geophysical Research Letters*, *52*(11), e2024GL114248. https://doi.org/10.1029/2024GL114248

Nakamura, S., Omura, Y., Kletzing, C., & Baker, D. N. (2019). Rapid precipitation of relativistic electron by EMIC rising-tone emissions observed by the Van Allen Probes. *Journal of Geophysical Research: Space Physics*, *124*(8), 6701–6714. https://doi.org/10.1029/2019JA026772

Newnham, D. A., Rodger, C. J., Marsh, D. R., Hervig, M. E., & Clilverd, M. A. (2020). Spatial distributions of nitric oxide in the antarctic wintertime middle atmosphere during geomagnetic storms. *Journal of Geophysical Research: Space Physics*, *125*(7), e2020JA027846. https://doi.org/10.1029/2020JA027846

Nikolaeva, V., Gordeev, E., Sergienko, T., Makarova, L., & Kotikov, A. (2021). AIM-E: E-region auroral ionosphere model. *Atmosphere*, *12*(6), 748. https://doi.org/10.3390/atmos12060748

Northrop, T. G., & Teller, E. (1960). Stability of the adiabatic motion of charged particles in the earth's field. *Physical Review*, *117*(1), 215–225. https://doi.org/10.1103/PhysRev.117.215

Paulikas, G. A. (1975). Precipitation of particles at low and middle latitudes. *Review of Geophysics*, *13*(5), 709–734. https://doi.org/10.1029/RG013i005p00709

Powell, K. G., Roe, P. L., Linde, T. J., Gombosi, T. I., & De Zeeuw, D. L. (1999). A solution-adaptive upwind scheme for ideal magnetohydrodynamics. *Journal of Computational Physics*, *154*(2), 284–309. https://doi.org/10.1006/jcph.1999.6299

Qiu, L., & Liu, H. (2025). Sporadic-E layer responses to super geomagnetic storm 10–12 May 2024. *Geophysical Research Letters*, *52*(8), e2025GL115154. https://doi.org/10.1029/2025GL115154

21699402, 2026, 8, Downloaded from https://agupubs.onlinelibrary.wiley.com/doi/10.1029/2026JA035200 by Center For Space Science And Applied Research, CAS, Wiley Online Library on [19/11/2026]. See the Terms and Conditions (https://onlinelibrary.wiley.com/terms-and-conditions) on Wiley Online Library for rules of use; OA articles are governed by the applicable Creative Commons License

Qiu, L., Liu, H., & Yu, T. (2025). Mechanism for sporadic E enhancement during the May 2024 geomagnetic storm: TIEGCM simulation. *Journal of Geophysical Research: Space Physics*, *130*(9), e2025JA034455. https://doi.org/10.1029/2025JA034455

Reinisch, B. W., Galkin, I. A., Khmyrov, G. M., Kozlov, A. V., Bibl, K., Lisysyan, I. A., et al. (2009). The new Digisonde for research and monitoring applications. *Radio Science*, *44*(1). https://doi.org/10.1029/2008RS004115

Resende, L. C. A., Batista, I. S., Denardini, C. M., Batista, P. P., Carrasco, A. J., Andrioli, V. F., & Moro, J. (2017). Simulations of blanketing sporadicE layer over the Brazilian sector driven by tidal winds. *Journal of Atmospheric and Solar-Terrestrial Physics*, *154*, 104–114. https://doi.org/10.1016/j.jastp.2016.12.012

Resende, L. C. A., Shi, J. K., Denardini, C. M., Batista, I. S., Picanço, G. A., Moro, J., et al. (2021). The impact of the disturbed electric field in the sporadic E (Es) layer development over Brazilian Region. *Journal of Geophysical Research: Space Physics*, *126*(12), e2020JA028598. https://doi.org/10.1029/2020JA028598

Resende, L. C. A., Zhu, Y., Chagas, R. A. J., Denardini, C. M., Espinosa, K. V. S., Chen, S. S., et al. (2025). Extra ionization causing the anomalous auroral sporadic E layer (Esa) over the equatorial Brazilian region during the recovery phase of the magnetic storm on 10 May 2024. *Space Weather*, *23*(12), e2025SW004669. https://doi.org/10.1029/2025SW004669

Resende, L. C. A., Zhu, Y., Denardini, C. M., Chagas, R. A. J., Da Silva, L. A., Andrioli, V. F., et al. (2023). Analysis of the different physical mechanisms in the atypical sporadic E (Es) layer occurrence over a low latitude region in the Brazilian sector. *Frontiers in Astronomy and Space Sciences*, *10*, 1193268. https://doi.org/10.3389/fspas.2023.1193268

Resende, L. C. A., Zhu, Y., Santos, A. M., Chagas, R. A. J., Denardini, C. M., Arras, C., et al. (2024). Nocturnal sporadic cusp-type layer (esc) resulting from anomalous excess ionization over the SAMA region during the extreme magnetic storm on 11 May 2024. *Journal of Geophysical Research: Space Physics*, *129*(11), e2024JA033167. https://doi.org/10.1029/2024JA033167

Ridley, A., De Zeeuw, D., Manchester, W., & Hansen, K. (2006). The magnetospheric and ionospheric response to a very strong interplanetary shock and coronal mass ejection. *Advances in Space Research*, *38*(2), 263–272. https://doi.org/10.1016/j.asr.2006.06.010

Rodger, C. J., Kavanagh, A. J., Clilverd, M. A., & Marple, S. R. (2013). Comparison between POES energetic electron precipitation observations and riometer absorptions: Implications for determining true precipitation fluxes. *Journal of Geophysical Research: Space Physics*, *118*(12), 7810–7821. https://doi.org/10.1002/2013JA019439

Roederer, J. G. (1970). Dynamics of geomagnetically trapped radiation. In J. G. Roederer & J. Zahringer (Eds.), *Physics and chemistry in space* (Vol. 2, p. 166). Springer.

Rong, P. P., Russell III, J. M., Mlynczak, M. G., Remsberg, E. E., Marshall, B. T., Gordley, L. L., & Lopez-Puertas, M. (2009). Validation of thermosphere ionosphere mesosphere energetics and dynamics/sounding of the atmosphere using broadband emission radiometry (TIMED/SABER) v1.07 ozone at 9.6 mm in altitude range 15 – 70 km. *Journal of Geophysical Research*, *114*(D4), D04306. https://doi.org/10.1029/2008JD010073

Russell, I. I. I. J. M., Mlynczak, M. G., Gordley, L. L., Tansock, J. J., & Esplin Jr., R. W., (1999). Overview of the SABER experiment and preliminary calibration results in Proceedings of the SPIE. In A. M. Larar (Ed.), *44th annual meeting, 18–23 July* (pp. 277–288). https://doi.org/10.1117/12.366382

Santos, A. M., Abdu, M. A., Souza, J. R., Sobral, J. H. A., Batista, I. S., & Denardini, C. M. (2016). Storm time equatorial plasma bubble zonal drift reversal due to disturbance Hall electric field over the Brazilian region. *Journal of Geophysical Research: Space Physics*, *121*(6), 5594–5612. https://doi.org/10.1002/2015JA022179

Santos, A. M., Batista, I. S., Brum, C. G. M., Sobral, J. H. A., Abdu, M. A., & Souza, J. R. (2021). F Region electric field effects on the intermediate layer dynamics during the evening prereversal enhancement at equatorial region over Brazil. *Journal of Geophysical Research-Space Physics*, *126*(3), e2020JA028429. https://doi.org/10.1029/2020ja028429

Santos, A. M., Batista, I. S., Sobral, J. H. A., Brum, C. G. M., Abdu, M. A., & Souza, J. R. (2020). Some differences in the dynamics of the intermediate descending layers observed during periods of maximum and minimum solar flux. *Journal of Geophysical Research: Space Physics*, *125*(10), e2019JA027682. https://doi.org/10.1029/2019JA027682

Santos, A. M., Brum, C. G. M., Batista, I. S., Sobral, J. H. A., Abdu, M. A., & Souza, J. R. (2022). Responses of intermediate layers to geomagnetic activity during the 2009 deep solar minimum over the Brazilian low-latitude sector. *Annales Geophysicae*, *40*(3), 259–269. https://doi.org/10.5194/angeo-40-259-2022

Sinnhuber, M., Nieder, H., & Wieters, N. (2012). Energetic particle precipitation and the chemistry of the mesosphere/lower thermosphere. *Surveys in Geophysics*, *33*(6), 1281–1334. https://doi.org/10.1007/s10712-012-9201-3

Stone, E. C., Frandsen, A. M., Mewaldt, R. A., Christian, E. R., Margolies, D., Ormes, J. F., & Snow, F. (1998). The advanced composition explorer. *Space Science Reviews*, *86*(1/4), 1–22. https://doi.org/10.1023/A:1005082526237

Tartaglione, N., Toniazzo, T., Orsolini, Y., & Otterå, O. H. (2020). Impact of solar irradiance and geomagnetic activity on polar NOx, ozone and temperature in WACCM simulations. *Journal of Atmospheric and Solar-Terrestrial Physics*, *209*, 105398. https://doi.org/10.1016/j.jastp.2020.105398

Toffoletto, F., Sazykin, S., Spiro, R., & Wolf, R. (2003). Inner magnetospheric modeling with the rice convection model. *Space Science Reviews*, *107*(1–2), 175–196. https://doi.org/10.1023/A:1025532008047

Tóth, G., Holst, B. V. D., Sokolov, I. V., De Zeeuw, D. L., Gombosi, T. I., et al. (2012). Adaptive numerical algorithms in space weather modeling. *Journal of Computational Physics*, *231*(3), 870–903. https://doi.org/10.1016/j.jcp.2011.02.006

Tóth, G., Sokolov, I. V., Gombosi, T. I., Chesney, D. R., Clauer, C. R., De Zeeuw, D. L., et al. (2005). Space weather modeling framework: A new tool for the space science community. *Journal of Geophysical Research*, *110*(A12), A12226. https://doi.org/10.1029/2005JA011126

Turner, D. L., Angelopoulos, V., Li, W., Bortnik, J., Ni, B., Ma, Q., et al. (2014). Competing source and loss mechanisms due to wave-particle interactions in earth's outer radiation belt during the 30 September to 3 October 2012 geomag-netic storm. *Journal of Geophysical Research: Space Physics*, *119*, 1960–1979. https://doi.org/10.1002/2014JA019770

Turner, D. L., Kilpua, E. K. J., Hietala, H., Claudepierre, S. G., O'Brien, T. P., Fennell, J. F., et al. (2019). The responseof earth's electron radiation belts togeomagnetic storms: Statistics from theVan Allen Probes era including effectsfrom different storm drivers. *Journal of Geophysical Research: Space Physics*, *124*(2), 1013–1034. https://doi.org/10.1029/2018JA026066

Vampola, A. L., & Gorney, D. J. (1983). Electron energy deposition in the middle atmosphere. *Journal of Geophysical ResearchSpace*, *88*.

Yi, S., Liu, N., Xie, Y., He, Z., Yu, J., & Cui, J. (2024). Frequency-drifting plasmaspheric hiss: A statistical study from the Van Allen Probes data. *Geophysical Research Letters*, *51*(8), e2024GL108448. https://doi.org/10.1029/2024GL108448

21699402, 2026, 8, Downloaded from https://agupubs.onlinelibrary.wiley.com/doi/10.1029/2026JA035200 by Center For Space Science And Applied Research, CAS, Wiley Online Library on [19/11/2026]. See the Terms and Conditions (https://onlinelibrary.wiley.com/terms-and-conditions) on Wiley Online Library for rules of use; OA articles are governed by the applicable Creative Commons License